Heat release rate estimation in laminar premixed flames using laser-induced fluorescence of CH$_2$O and H-atom

Irfan A. Mulla [a,1], Aadil Dowlut [a], Taaha Hussain [a], Zacharias M. Nikolaou [b], Satyanarayanan R. Chakravarthy [c], Nedunchezhian Swaminathan [b], Ramanarayanan Balachandran [a,*]

[a] *Department of Mechanical Engineering, University College London, Torrington Place, London WC1E 7JE, UK*
[b] *Department of Engineering, Cambridge University, Trumpington Street, Cambridge CB2 1PZ, UK*
[c] *Department of Aerospace Engineering, Indian Institute of Technology Madras, Chennai 600036, India*

ABSTRACT

The present work demonstrates the feasibility of heat release rate imaging using the laser-induced fluorescence (LIF) of atomic hydrogen (H-atom) and formaldehyde (CH$_2$O) in laminar premixed flames. The product of H-atom LIF and CH$_2$O LIF signals is evaluated on a pixel-by-pixel basis and is compared with that of the OH $\times$ CH$_2$O technique. These results for equivalence ratio ranging from 0.8 to 1.1 are compared with computations of one-dimensional freely-propagating flames. The performance of these markers is studied based on the following two aspects: the spatial accuracy of the local heat release rate and the trend in the total heat release rate with equivalence ratio. The measured trend in the spatial distribution of radicals and the deduced heat release rate agree well with the computational values. The variation in the spatially integrated heat release rate as a function of equivalence ratio is also investigated. The results suggest that the trend in the variation of the integrated heat release rate and the spatial location of heat release rate can be evaluated by either of these markers. The OH-based marker showed certain sensitivity to the chemical mechanism as compared to the H-atom based marker. Both the OH-based and H-atom based techniques provide close estimates of heat release rate. The OH based technique has practical advantage when compared to the H-atom based method, primarily due to the fact that the H-atom LIF is a two-photon process.

1. Introduction

The heat release rate (HRR) is one of the important properties of the combustion process, as it characterises the extent of energy conversion from chemical potential to thermal energy. The spatial distribution of heat release rate can provide locations of reaction zones, which may be used to identify the hot spots that lead to uncontrolled ignition in internal combustion engines [1] and non-uniform pattern factors in gas turbines [2]. The HRR is vital for understanding and predicting combustion instability [3–7] and combustion noise [8–9] in gas turbine engines. The direct measurement of HRR or a quantity that fully represents HRR is not practical yet because of the challenges involved in measuring many tens of species and temperature simultaneously. Instead, certain reliable chemical markers (radicals) [7,10–14] or indicators (dilatation) [10] that correlate well with the heat release rate have been employed.

The indirect measurement of HRR is performed using both natural chemiluminescence from the flame and laser induced fluorescence (LIF) from excited radicals. The chemiluminescence measurement is relatively simple, whereas LIF measurement requires sophisticated lasers to excite specific species, such as OH, CH, CH$_2$O or HCO. Yet, the LIF measurement provides planar spatial resolution free from line-of-sight integration of the signal, unlike chemiluminescence. In practical combustion devices, LIF based measurements are generally not possible and hence, the preferred strategy is to use chemiluminescence. On the other hand, for fundamental studies in laboratory burners, LIF has been used where measurement accuracy outweighs complexity. Hence, both LIF- and chemiluminescence based HRR measurements are widely reported as summarised next.

* Corresponding author. Fax: +44 2073880180.
  E-mail addresses: irfanmulla.ae@gmail.com (I.A. Mulla),
r.balachandran@ucl.ac.uk, r_balachndrn@meng.ucl.ac.uk (R. Balachandran).
[1] On research exchange from Indian Institute of Technology Madras, India. Presently at CORIA - UMR 6614, CNRS, INSA de Rouen, 76801 Saint-Étienne-du-Rouvray, France

The intensities of chemiluminescent emission from CH*, OH* and CO$_2$* are reported to increase linearly with fuel flow rates for a given equivalence ratio [11]. Hardalupas and Orain [12] examined chemiluminescence from different radicals to find reliable indicators of HRR. They report that chemiluminescent emission from CH*, OH* and CO$_2$* radicals are all good indicators of HRR. The authors [12] used a Cassegrain telescope to limit the collection angle, thus increasing the spatial resolution. Though this collection optics increases the in-plane spatial resolution, yet the chemiluminescence method itself is not free from line-of-sight integration of the signal. Hardalupas et al. [13] developed HRR and equivalence ratio sensor based on chemiluminescence techniques. The CH* and OH* signals are simultaneously acquired using the Cassegrain telescope. The authors [13] validated the spatial distribution of the HRR in a laminar flame using a LIF based measurement technique. The peak location of HRR was in good agreement with the LIF based measurements, yet the spatial distribution of HRR deduced from chemiluminescence was not in agreement with the LIF based measurements.

Similar to the chemiluminescence based measurements, the LIF based measurements also require reliable markers of HRR. Najm et al. [14] carried out detailed computational and experimental studies to find suitable markers. They also discussed in detail the adequacy of the chemiluminescence based measurements. They found OH* and CH* to be unreliable indicators of local extinction. Their results suggested that the HCO mole fraction to be a reliable marker of HRR. These authors [14] demonstrated the feasibility of and illustrated issues associated with imaging HCO using PLIF. The fluorescence signal was not strong enough for single-shot imaging, and as a result 100 images were averaged to achieve a signal-to-noise ratio (SNR) of 2. The PLIF signal from HCO is generally weak due to its low concentration, low quantum yield of its fluorescence, and short fluorescence time scales [7,14,15]. Kiefer et al. [15] have recently demonstrated the feasibility of single-shot PLIF imaging of the HCO radical. They employed a long pulsed and broadband alexandrite laser providing higher fluorescence signal than the conventional Nd:YAG and dye laser system. Zhou et al. [16] extended this study further with detailed investigation to enable single-shot HCO PLIF imaging. The authors identified interference-free excitation wavelength and laser fluence (energy per unit area) limit to reduce photolytically generated HCO. This technique is limited to lean premixed flames, because in rich flames significant interference from large hydrocarbons is reported.

To circumvent the difficulties associated with HCO PLIF, an alternative strategy was developed by Paul and Najm [10]. They used the pixel-by-pixel product of simultaneously obtained CH$_2$O and OH PLIF images. This strategy is based on a presumption that the HCO radical forms through CH$_2$O + OH → HCO + H$_2$O. The authors [10] validated this technique by comparing the correlation between the following computed quantities: HRR, HCO concentration and the product of CH$_2$O and OH concentrations for stoichiometric and rich flames. The comparison showed good spatial and temporal correlations between all three quantities. This method facilitated the possibility of single-shot measurements. Additionally, the spatial concentrations of CH$_2$O and OH can be extracted from the PLIF images. In order to obtain quantitative information from such measurements the temperature dependence of the LIF signals has to be carefully considered. As noted by Paul and Najm [10], the product of the LIF signals primarily depends on the product of the concentrations in the region of overlap between CH$_2$O and OH where a narrow range of temperature is expected. This argument is further substantiated by Ayoola et al. [7]. Numerous studies have demonstrated the applicability of this technique for premixed and non-premixed flames in various geometrical configurations and flow conditions. The applicability of this diagnostic technique was demonstrated by Böckle et al. [17] in turbulent premixed flames

in Bunsen and swirl configurations. This technique was also used by Balachandran et al. [18] and Ayoola et al. [7] to investigate responses of turbulent premixed flames to imposed velocity fluctuations. The reliability of this technique in non-premixed flames has been demonstrated by Gordon et al. [19] while investigating autoignition events in transition at the base of lifted flames. Recently, this technique was implemented to image reaction zones near blow-off conditions in a bluff-body stabilised turbulent methane–air premixed flames [20] and in a swirl-stabilised turbulent n-heptane spray flames [21]. This method has also been assessed by Fayoux et al. [22] by comparing measured and computed HRR in counter-flow laminar premixed flames. These authors [22] conclude that the product of simultaneous CH$_2$O and OH PLIF is a reliable technique to deduce HRR. The width of experimental OH × CH$_2$O profile is reported [22] to be larger than that of the computed profile. It has to be noted that the above correlation was validated for laminar premixed methane flames.

Gazi et al. [23] assessed the adequacy of the OH × CH$_2$O marker (based on mole fraction) for a wide range of fuels, and concluded that the extension of these markers to other fuels and stoichiometries should be performed with caution. They remarked that alternative correlations between HRR and chemical markers may exist for a given flame. Minamoto and Swaminathan [24] reconstructed synthetic PLIF signals using data from direct numerical simulations. The synthetic PLIF signals were examined to assess the adequacy for their use as the heat release rate markers for MILD combustion of methane. They concluded that use of only OH, CH$_2$O or HCO PLIF signal does not reliably represent HRR, whereas the OH × CH$_2$O PLIF based technique is found to be adequate.

Recently, Nikolaou and Swaminathan [25] re-examined the [OH] × [CH$_2$O] product based HRR correlation (where '[-]' denote molar concentrations) for methane, methane diluted with combustion products, and for other multi-component fuels, such as blast furnace gas. They found that HRR correlations varied strongly with stoichiometry and fuel composition. For methane–air flames, alternative markers were suggested for lean to stoichiometric mixtures, including species such as H, CH$_2$O, O, and CH$_4$. These markers were studied using both laminar flame calculations and DNS data of turbulent premixed flames, and were found to have a better correlation with the HRR than the OH × CH$_2$O marker. In particular, it was shown that [25], for equivalence ratios between 0.6 and 1.0, the HRR correlates better with the forward rate of the reaction H + CH$_2$O → HCO + H$_2$O, whereas for a multi-component fuel, even a two-scalar based marker is inadequate. It is important to note that, for methane–air flames, HCO forms not only through OH + CH$_2$O → HCO + H$_2$O but through H + CH$_2$O → HCO + H$_2$ as well [25].

In the light of these observations, the objective here is to investigate the feasibility of the H × CH$_2$O LIF technique and to compare this with the OH × CH$_2$O LIF correlation in laminar methane-air premixed flames in a Bunsen configuration as a first step. This paper is organised as follows. The experimental details of the burner and the laser diagnostic techniques are provided in the next section (Section 2), followed by the data analysis methods. The results pertaining to the spatial distribution of HRR and the integrated HRR evaluated from both H × CH$_2$O and OH × CH$_2$O LIF techniques are discussed in Section 3. The conclusions of this work are summarised along with the future scope in the last section (Section 4).

2. Experimental details and data analysis

2.1. Burner and flame conditions

The premixed laminar methane–air flames are stabilised on an axi-symmetric Bunsen burner of 10 mm nozzle diameter. The
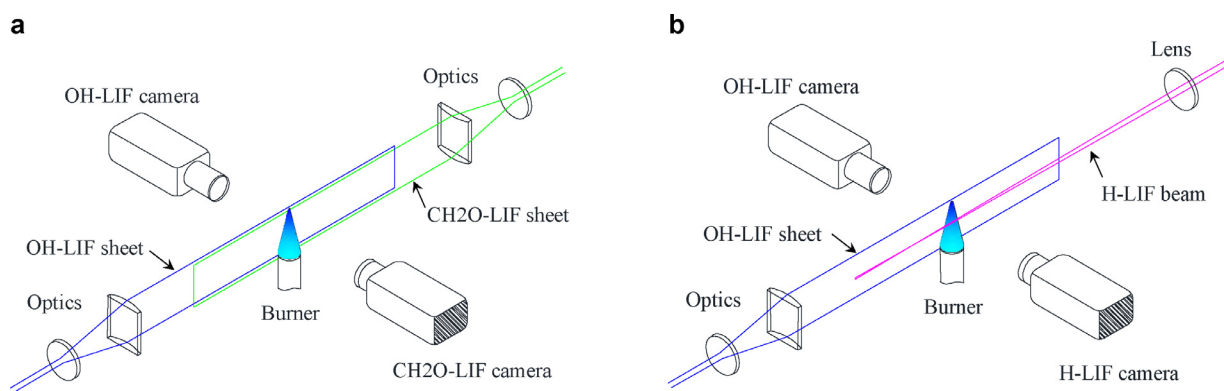
Fig. 1. Laser diagnostic systems: (a) simultaneous OH/CH$_2$O LIF set-up, and (b) simultaneous OH/H-atom LIF set-up.

Bunsen burner configuration facilitates one-dimensional (1D) measurements, such as the H-atom LIF performed using a beam instead of a planar light sheet. Such one-dimensional measurements are preferred when the SNR is low with the planar light sheet. The H-atom LIF set-up is illustrated in Fig. 1. Flames with equivalence ratio ϕ = 0.8, 0.9, 1.0, 1.1 and bulk velocity V = 0.4, 0.9, 1.2, 1.2 m/s respectively are investigated. For a given equivalence ratio, the bulk velocity is adjusted to obtain a stable flame. The air and methane flow rates are metered with thermal flow-meters (Vögtlin Instruments) and controlled through high precision needle valves. The accuracy of the present flow rates varies from ± 0.8 to ± 2.3% depending on the flow rates relative to the full scale of the flow-meters.

2.2. Diagnostic details

In the present work, the product of OH and CH$_2$O LIF signals is evaluated using a simultaneous PLIF imaging system. Figure 1(a) shows the schematic of simultaneous OH/CH$_2$O LIF system.

The OH radical is excited at ~283 nm. The Q_1(6) line in the $A^2\Sigma^+ - X^2\Pi$ (1, 0) band is excited. This transition is chosen following a previous study on HRR imaging [7]. A frequency-doubled Nd:YAG laser (Litron, NanoPIV model) is used to pump a tunable dye laser (Fine Adjustments, Pulsare-S model) containing rhodamine 6G dye. The fundamental wavelength from the dye laser is frequency-doubled and tuned to generate 283 nm with ~12 mJ pulse energy. The laser beam is spatially filtered similar to [7], and thus, only a central portion containing 4 mJ pulse energy is used to ensure that the LIF signal is not saturated. The spatially filtered beam is converted into a light sheet using a plano-concave cylindrical lens and focused by a bi-convex spherical lens. The resulting light sheet is 30 mm in height and ~0.2 mm in thickness. The PLIF signal is amplified by a UV intensifier and imaged using a CCD camera (TSI, pixel resolution 1376×1024). The camera is equipped with a UV lens and a set of UG11 and WG305 SCHOTT filters to collect the signal around 310 nm within the wavelength range of 300–375 nm. The background flame chemiluminescence is suppressed by gating the camera to 300 ns.

Following a recent study [20], the $A^2A_1 - X^1A_1$ 4_0^1 pQ (J'' = 15, K'' = 5) transition of CH$_2$O is excited near 355 nm. The 355 nm wavelength is generated from a frequency-tripled Nd:YAG laser (Litron, LPY 7864-10 model). The beam with pulse energy of ~200 mJ is expanded into a light sheet by combination of a plano-concave cylindrical lens and a bi-convex spherical lens. The light sheet is 25 mm in height and ~0.3 mm in thickness. The linearity of the LIF signal in the present system is verified. The PLIF signal is intensified by a visible intensifier and collected using a CCD camera (TSI, pixel resolution 1376×1024). A combination of GG 395 and BG 40 filters is used to filter the PLIF signal in the range of

395–610 nm. Similar to the OH-PLIF system, the camera is gated to 300 ns. The 283 nm and 355 nm pulses are separated by 500 ns. The synchronisation between the laser pulses, camera exposure, and the intensifier gate is controlled through a synchroniser. The data is acquired using the Insight® software package (TSI).

The LIF of H-atom and CH$_2$O could not be performed simultaneously because the required PLIF systems were unavailable in this laboratory. Instead, two separate experiments were performed; namely, the simultaneous OH/CH$_2$O LIF and the simultaneous OH/H LIF. As the flames considered in this study are laminar, the data can be statistically conditioned to obtain quasi-simultaneous mean H/CH$_2$O LIF signals.

Figure 1(b) illustrates a schematic of the simultaneous OH/H LIF system. The excitation and detection schemes for atomic hydrogen are followed from [26,27]. The H-atom LIF is obtained via a two-photon excitation scheme. Atomic hydrogen is excited via the $(3s \; ^2S, \; 3d \; ^2D) \leftarrow\leftarrow 1s \; ^2S$ transitions near 205 nm, and the resulting fluorescence is collected from the H($n = 3$) $\rightarrow$ H($n = 2$) transitions at 656 nm. The H-atom LIF signal is filtered using a narrowband filter with centre wavelength of 655 nm and a bandwidth of 15 nm. The Nd:YAG pumped dye laser running rhodamine 101 dye is tuned to generate ~615 nm. This fundamental wavelength is frequency tripled to generate ~205 nm. For this excitation scheme, variations in the temperature-dependent quenching rate are estimated to have a minor contribution [28]. Unlike the OH and CH$_2$O PLIF system, the PLIF signal from the H-atom is not observed when the beam is converted to a light sheet at the fluence of ~0.01 J/cm^2. Hence, following previous works [26–30], a focused laser beam is used, which provides the LIF signal along a line. The beam is focused using a 500 mm focal length spherical lens. The beam diameter measures ~ 0.3 mm at the measurement location. The average beam energy is ~0.75 mJ, which provides a laser fluence of ~1 J/cm^2. This fluence level is used in order to obtain a good SNR with the available collection system. The SNR measured at the peak value in an instantaneous realisation is typically 18 for ϕ = 1.1. However, an SNR of 9 is estimated at the location of intersection of the CH$_2$O and H-atom profiles. Similarly, the SNR evaluated at other equivalence ratio (ϕ = 0.8 to 1.1) varies from 5 to 9. The past work of Kulatilaka et al. [29] provides details on the characteristics of H-atom LIF signals at different fluence levels. The photolytic interference from the CH$_3$ radical is reported [26,29] at higher laser fluence. As observed from the results in [29], these interference effects are dominant in the post-flame region. However, towards the reactant side, on the rising edge of the H-atom profile, the interference effects are minimal. In the present work, only the rising edge of the H-atom profile contributes towards the estimation of HRR, as will be discussed later in Section 3.1. Hence, the photolytic interference is not expected to have significant contribution to the HRR evaluation.

Table 1
Premixed flame conditions investigated in the present study.

No.	ϕ	V (m/s)	H (mm)	h (mm)	θ_h (deg)	T_{pk} (K)	N	dx_N (mm)	dx (mm)
1	0.8	0.4	9	3.5	30	2000	158	0.25	0.35
2	0.9	0.9	19	9.0	15	2140	190	0.17	0.20
3	1.0	1.2	23	9.0	13	2230	197	0.19	0.19
4	1.1	1.2	22	9.0	15	2210	195	0.19	0.22

ϕ = equivalence ratio, V = bulk velocity, H = height of the flame tip from the nozzle, h = profile extraction height above the nozzle, θ_h = local flame inclination angle at h with respect to the vertical axis of the nozzle, T_{pk} = peak temperature of the modelled flame, N = number of retained realisations, dx_N = RMS of flame location fluctuations at h over the retained realisations, dx = RMS of flame location fluctuations at h over the total of 200 realisations.

2.3. Data reduction procedures

The PLIF images are acquired on two different camera systems as described in the previous sub-section. It is crucial to overlap the two fields of views on a pixel-by-pixel basis to evaluate HRR. To ensure this overlap, a method similar to that presented in [7,18] is adopted. A calibration target image is acquired on both cameras. A transformation matrix is generated by tracking identical points in the target images captured by both cameras. The images are matched to sub-pixel accuracy, which is verified from the transformed calibration target. The transformed images are resized by using 2 × 2 binning. The resolution after the binning is 55 μm/pixel. After background correction, the PLIF images are median-filtered with 3 × 3 pixel window to reduce noise. The LIF profiles at a height h are extracted from the instantaneous PLIF images. The height H of the flame tip from the nozzle and the profile extraction height h are listed in Table 1. For each experiment, 200 realisations are acquired. A few of these realisations are discarded owing to minute shot-to-shot flame fluctuations. These fluctuations may be attributed to mild flow rate fluctuations within the accuracy of the flow-meters. The flame location is determined by following the maximum gradient in the OH LIF profile. The extent of these shot-to-shot flame fluctuations is characterised by evaluating the root-mean-squared (RMS) values of the fluctuations in the flame location dx at the measurement height over the 200 realisations, as listed in Table 1. The profiles that lie within 15% of the mean flame location are retained. The number of retained realisations N for each of the flame conditions is also listed in Table 1. Additionally, the RMS of flame location fluctuations over the retained realisations dx_N is included in Table 1. Thus, the instantaneous profiles are averaged over at least 150 realisations in a flame-fixed frame of reference.

The profile extraction height h is illustrated on the respective mean OH-PLIF images in Fig. 2 for each of the equivalence ratios. As observed from these images, the profile extraction height is sufficiently away from the nozzle lip and the flame-tip. The light sheet appears to be fairly uniform along the x direction, for a given y. However, the effect of non-uniformity in the laser beam can be observed along the y direction, e.g., around $y = 12$ mm. The LIF profiles are extracted at $h = 9$ mm for $\phi = 0.9$, 1.0 and 1.1, whereas at $h = 3.5$ mm for $\phi = 0.8$. In the present work, the extracted mean profiles are corrected for the non-uniformity in the laser beam. Such correction is required only for $\phi = 0.8$, as the h is different in this case than the rest of the flames. The correction is performed in following manner: the peak LIF signal along the shoulder of the $\phi = 0.9$ flame is extracted in the region of $y = 3$ to 10 mm from the mean OH-PLIF image. Within this range of y, the flame front is not significantly curved, and hence, the flame characteristics are expected to be nearly constant. The extracted LIF profile is smoothened with a polynomial fit to a correlation coefficient of > 0.99. The ratio of the LIF signals at $y = 9$ mm and 3.5 mm is evaluated. This ratio is used to correct the signal at $y = 3.5$ mm of the $\phi = 0.8$ flame to account for the non-uniformity in the beam profile. A similar correction scheme is also implemented for the CH_2O LIF profile.

The extracted LIF profiles are not in the normal direction to the flame front. Hence, the spatial profiles are corrected to account for the flame front inclination. The local flame front angle θ_h at the height h with respect to the vertical axis of the nozzle is deduced from the mean OH-PLIF image, and listed in Table 1 for each ϕ. Subsequently, the distances are corrected using trigonometric relations to account for the non-normal flame front angle. This is validated by evaluating the OH profile in a direction normal to the flame front. The profile extracted normal to the flame front along line-A (see inset image in Fig. 3) and the corrected profile using data along line-B agree very well. The profiles are presented in a peak-fixed frame of reference. All the profiles for each of the flames are similarly corrected.

As mentioned earlier, two sets of experiments are performed to yield the OH/CH_2O PLIF and OH/H PLIF. The OH PLIF is common between these two experiments, and is used as a marker of the flame location for the purpose of data processing. It is ensured that the rising edges of the OH-profile across the flame front in both the experiments (OH/CH_2O and OH/H) overlap spatially. In
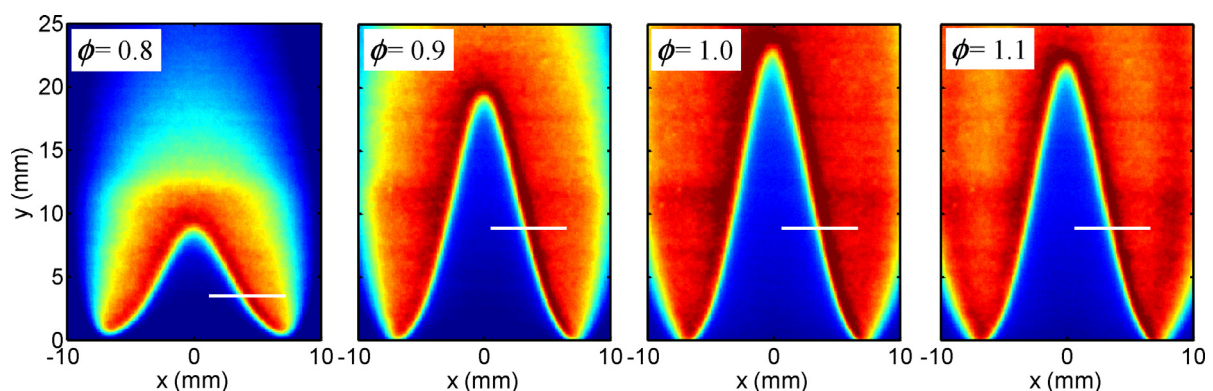

Fig. 2. Mean OH-PLIF images and respective flame extraction heights indicated by white lines for different equivalence ratios.
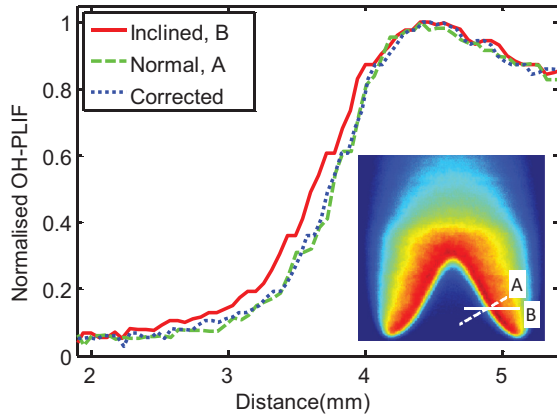
Fig. 3. OH profile correction for non-normal flame inclination for $\phi = 0.8$ flame. The inset shows the mean OH-PLIF image (20 mm × 20 mm). The profile measured along the solid white line-B is not normal to the flame front (inclined). The normal profile is plotted along the broken white line-A shown on the OH-PLIF image in the inset. The point of intersection of the two lines is 3.5 mm above the nozzle. The radial distance is measured from the nozzle axis.

this way, the spatial distributions of all the three radicals are obtained in a quasi-simultaneous manner.

The HRR is estimated based on both OH/CH$_2$O and H/CH$_2$O by taking the pixel-by-pixel products along the profiles. The areas under the OH × CH$_2$O and H × CH$_2$O curves are used to estimate the spatially integrated HRRs.

2.4. Simulation details

One-dimensional, freely-propagating laminar flames at a pressure of 1 atm and reactant temperature of 298 K are modelled using the PREMIX code of the CHEMKIN package [31]. The GRI Mech 3.0 [32] is used for chemical kinetics in the computations, since it is a well-validated mechanism for methane–air combustion. This model is good for capturing flame structure in regions away from the central curved region of a Bunsen laminar flame. The various transport coefficients are specified using the mixture-averaged formulation. The changes in the flame speed, thermal thickness, and structure were found to be negligible when a detailed multi-component formulation for diffusion coefficients was used. The use of the mixture-averaged formulation results in considerable savings of computational effort as it is well known. The GRAD and CURV parameters used for the simulations were 0.05 or lower to get a well-resolved flame structure and the spatial variations of important radicals and intermediate species required for the current analysis. It is worth noting that the chemical mechanism used for the simulations can influence the spatial variation of HRR and hence the robustness and validity of the HRR marker identified using numerical simulations. However, it was shown in [25] that the forward rate of the reaction H + CH$_2$O → HCO + H$_2$ contributes more to the total heat release rate as compared to the contribution from the rate of OH + CH$_2$O → HCO + H$_2$O irrespective of the chemical mechanism, the GRI Mech 3.0 and San Diego mechanisms [33], used in the calculation. This insensitivity to the relative contribution from H + CH$_2$O reaction to the overall heat release rate suggests that the marker [H] × [CH$_2$O] is insensitive to the chemical mechanism as compared to the [OH] × [CH$_2$O] marker. Elaborate discussion on these points can be found in [25], and therefore, the GRI Mech 3.0 is considered adequate for the purposes of this study.

2.5. Temperature dependence of LIF

The reaction rate and LIF signal intensity vary with temperature, and the HRR imaging technique assumes that these

dependencies are similar. Thus, the product of the LIF signals is believed to mimic the reaction rate. It is important to establish the extent to which this assumption is valid. A simplified analysis similar to that by Ayoola et al. [7] is performed below.

For the [OH] × [CH$_2$O] marker, the corresponding reaction is OH + CH$_2$O → HCO + H$_2$O. The forward rate of reaction for this reaction is k_1 [OH][CH$_2$O], where k_1 is the specific rate constant of Arrhenius form. Similarly, k_2 [H][CH$_2$O] indicates the forward rate of reaction corresponding to the [H] × [CH$_2$O] marker. These rate constants are evaluated from the laminar flame calculations explained in Section 2.4. The product of the LIF signals of OH and CH$_2$O is written as f_1 [OH][CH$_2$O], where f_1 indicates the combined effect of the temperature. Likewise, the product of the H-atom and CH$_2$O LIF signals is written as f_2 [H][CH$_2$O]. The HRR imaging technique assumes that $f(T)$ mimics $k(T)$ for the selected LIF transition, where (T) indicates the temperature dependence.

For a given concentration, the temperature dependence mainly arises from the collisional quenching and the Boltzmann population fraction. Following Eckeberth [34], the LIF signal intensity S_f can be written as

$$S_f \sim N_1 \, f_{B,1} B_{12} \frac{A_{21}}{A_{21} + Q_{21}} I_\nu \tag{1}$$

where, N_1 is the total number density of an excited species; $f_{B,1}$ is the Boltzmann population fraction of the lower electronic (pumped) state; B_{12} is the absorption coefficient; A_{21} is the spontaneous emission coefficient; Q_{21} is the collisional quenching rate; and, I_ν is the incident laser irradiance.

For the present LIF species (OH, CH$_2$O, and H-atom), $A_{21} << Q_{21}$ [34]; therefore, for a quenching dominated LIF, Eq. (1) can be simplified as

$$S_f \sim N_1 \, f_{B,1} B_{12} \frac{A_{21}}{Q_{21}} I_\nu \tag{2}$$

In the above equation, the temperature dependence appears through $f_{B,1}$ and Q_{21}, where the quenching rate is given by

$$Q_{21} = \sum_i N_i \sigma_i \, \nu_i \; = \sum_i N_i \hat{k}_i \tag{3}$$

where, N_i is the number density of collision species i; σ_i is the quenching cross-section by species i; and, ν_i is the relative velocity of the excited species and the collision partner i. The quenching rate coefficient $\hat{k}_i$ is the product $\sigma_i \nu_i$.

The temperature dependence of the number density scales as $N_i \propto T^{-1}$, whereas $\nu_i \propto T^{0.5}$. Thus, the term $N_i \nu_i \propto T^{-0.5}$. The quenching cross-section is $\sigma_i \propto T^\beta$, where the value of β is species-dependent. For CH$_2$O, the past work [7] assumes $\beta = 0$ and $\beta = -0.5$. In the present work, we assume $\beta = -0.25$; consequently, $Q_{21} \propto T^{-0.75}$. For H-atom, following the past work [27], we assume the quenching rate coefficient $\hat{k}_i$ to be temperature-independent, which leads to $Q_{21} \propto T^{-1}$. The quenching rate for OH LIF depends weakly on temperature for the typical range of interest [35,36]. The quenching rate varies by ~15% over the temperature range of 1300–1900 K [35]. This temperature range covers the region of significant overlap (characterised later in Section 3.1 as Δx) of the OH/CH$_2$O or OH/H-atom for the range of $\phi = 0.8$–1.1. Thus, in the present work, Q_{21} is assumed to be a constant for OH LIF, as has been done in [7].

The Boltzmann population depends on the choice of the excited transition line (wavelength). We estimate the Boltzmann population for OH following Ayoola [37], whereas for CH$_2$O, we follow the work of Kyritsis et al. [38], which uses the excitation near 355 nm similar to the present work. For the H-atom, the energy gap between the 1s and 2s orbital states is very large (~10.2 eV) relative to the k_bT term, where k_b is the Boltzmann constant. Thus, the Boltzmann population is expected to be nearly insensitive within a typical range of temperature variation across the flame

(A. Dreizler, personal communication). Consequently, in the present work, the Boltzmann population of the H-atom is assumed to be insensitive to temperature in the range of interest.

3. Results and discussion

3.1. Flame structure

The average LIF profiles of OH, H-atom and CH_2O are shown in Fig. 4 for the $\phi = 1.0$ flame. The origin of the x-axis is set to zero at the location where CH_2O peaks in each of the computed and the measured profiles. This facilitates comparison of the experimental and computational results in the same frame of reference. The range of the x-axis in the experiment (Fig. 4(a)) is scaled using a factor obtained from the ratio of the experimental LIF CH_2O profile's full width at half maximum (FWHM) to the corresponding computational width. Such scaling leads to clear representation of the profile, which would otherwise be spatially indistinguishable. The profiles are extracted at 9 mm above the nozzle and corrected for flame inclination as explained earlier. Note that the images of the simultaneous OH/CH_2O and simultaneous OH/H PLIF are acquired at two different instances. The profile marked as OH-1 is obtained from the simultaneous OH/CH_2O-PLIF experiment, whereas OH-2 is obtained from simultaneous OH/H-PLIF experiment. The OH/H LIF profiles are spatially translated to overlap OH-1 and OH-2 as observed from Fig. 4(a), thus acquiring OH, H and CH_2O in a quasi-simultaneous manner. This strategy is suitable for laminar flames on an averaged basis. For further processing, only one of the OH profiles (OH-1) is retained. The rising edge of the H-atom profile lies slightly ahead of that of the OH. The CH_2O profile reaches a peak and drops sharply. These trends are similar to those of the calculated profiles as shown in Fig. 4(b). However, the FWHM of the CH_2O LIF profile measures 1.9 times that of the calculated profile. This disagreement may be partly attributed to the fact that the calculations are performed for a freely-propagating premixed flame model, which does not exactly correspond to the conical Bunsen flame used in the experiments. Similar observation has been noted in a previous study [22], where the authors simulated the experimental conditions, yet the experimentally observed CH_2O LIF profile was found to be wider than the simulated CH_2O profile.

Furthermore, the slopes of the OH and the H-atom LIF profiles are not identical, as opposed to the calculation. This discrepancy between the experimental and calculated profiles may be attributed to the limited spatial resolution of the present experimental system. The projected pixel resolution in the present work is 55 μm; however, the true spatial resolution is governed by the thickness of the laser sheet or the diameter of the laser beam, either of which is 0.3 mm. The present measurements are uncertain to this extent, and the observed discrepancy is within this resolution. A greater separation between the OH LIF and H-atom LIF profiles could also be attributed to the conical geometry of the flame. The three-dimensional nature of the conical geometry is susceptible to errors originating from the minute misalignment in the laser sheets, if any present.

The HRR evaluated using both the products, $[OH] \times [CH_2O]$ and $[H] \times [CH_2O]$, are plotted in Fig. 5 for three equivalence ratios spanning from lean to rich regime. Similar to Fig. 4, for $\phi = 1.0$, the range of the x-axis in the experiment is scaled by the ratio of the experimental CH_2O LIF profile width to that of the simulation. These experimental and simulation x-axis ranges are retained across other equivalence ratios ($\phi = 0.9$ and 1.1) as well, for consistency.

Figures 5(a), (c), and (e) show the mean LIF profiles and the products of the LIF signals. The profiles are qualitatively similar across the equivalence ratios. Similar observation is noted for the calculated profiles as shown in Fig. 5(b), (d), and (f). The FWHM of the CH_2O profile in the calculations decreases from 0.38 to 0.31 mm over $\phi = 0.8$ to 1.1. A similar trend is noted in the measured CH_2O LIF profiles. However, the measured values are nearly twice as high as the calculated ones (0.80–0.59 mm over $\phi = 0.8$–1.1). The profiles of the measured CH_2O LIF signal and the calculated CH_2O concentration have a minimum width at $\phi = 1.1$. The trends in the experimentally evaluated HRR (i.e., the products of LIF signals, $OH \times CH_2O$ and $H \times CH_2O$) are in good agreement with the calculated products of the concentrations, $[OH] \times [CH_2O]$ and $[H] \times [CH_2O]$. The products of the LIF profiles, $OH \times CH_2O$ and $H \times CH_2O$, are observed to be broader than those of the calculations, similar to the observations reported by Fayoux et al. [22] in counter-flow premixed laminar flames. In the calculations, the $[H] \times [CH_2O]$ profile lies slightly ahead of the $[OH] \times [CH_2O]$ profile towards the reactant side, as observed from Fig. 5(b), (d), and (f). Similarly, in the experiments, the falling edge of the $H \times CH_2O$ LIF profile lies slightly ahead of the $OH \times CH_2O$ LIF profile. However, the rising edge of the $H \times CH_2O$ LIF profile lies slightly behind the $OH \times CH_2O$ LIF profile except near the peak region. This can be attributed to the uncertainty associated with the limited spatial resolution of the present experimental system. The $H \times CH_2O$ LIF profile appears smoother and slightly narrower than the $OH \times CH_2O$ LIF profile. This is most likely due to the higher intensities of the H-atom and CH_2O LIFs than that of the OH LIF with the present LIF system.
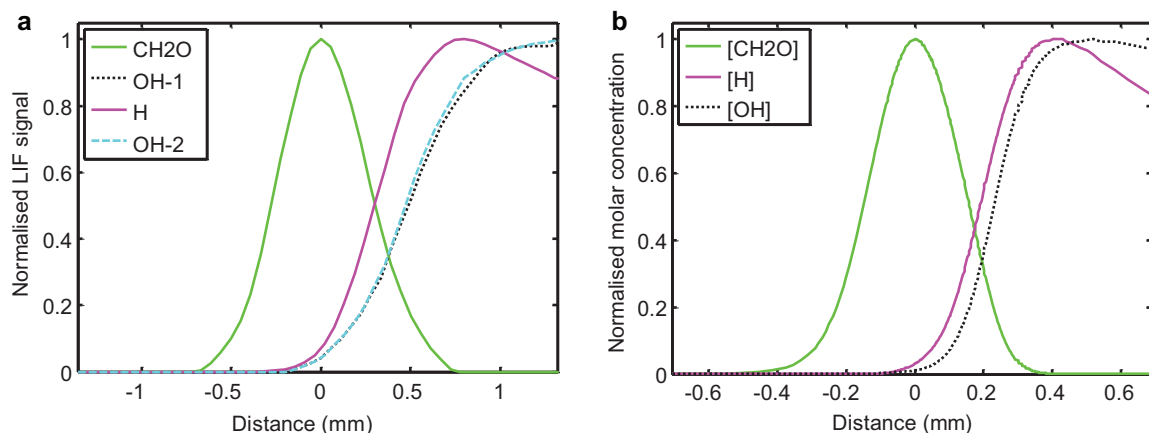

Fig. 4. Profiles of radicals for $\phi = 1.0$ flame. (a) experimental mean LIF profiles. The profile OH-1 is obtained simultaneously with CH_2O, whereas OH-2 is obtained simultaneously with H-atom. (b) calculated molar concentration profiles.
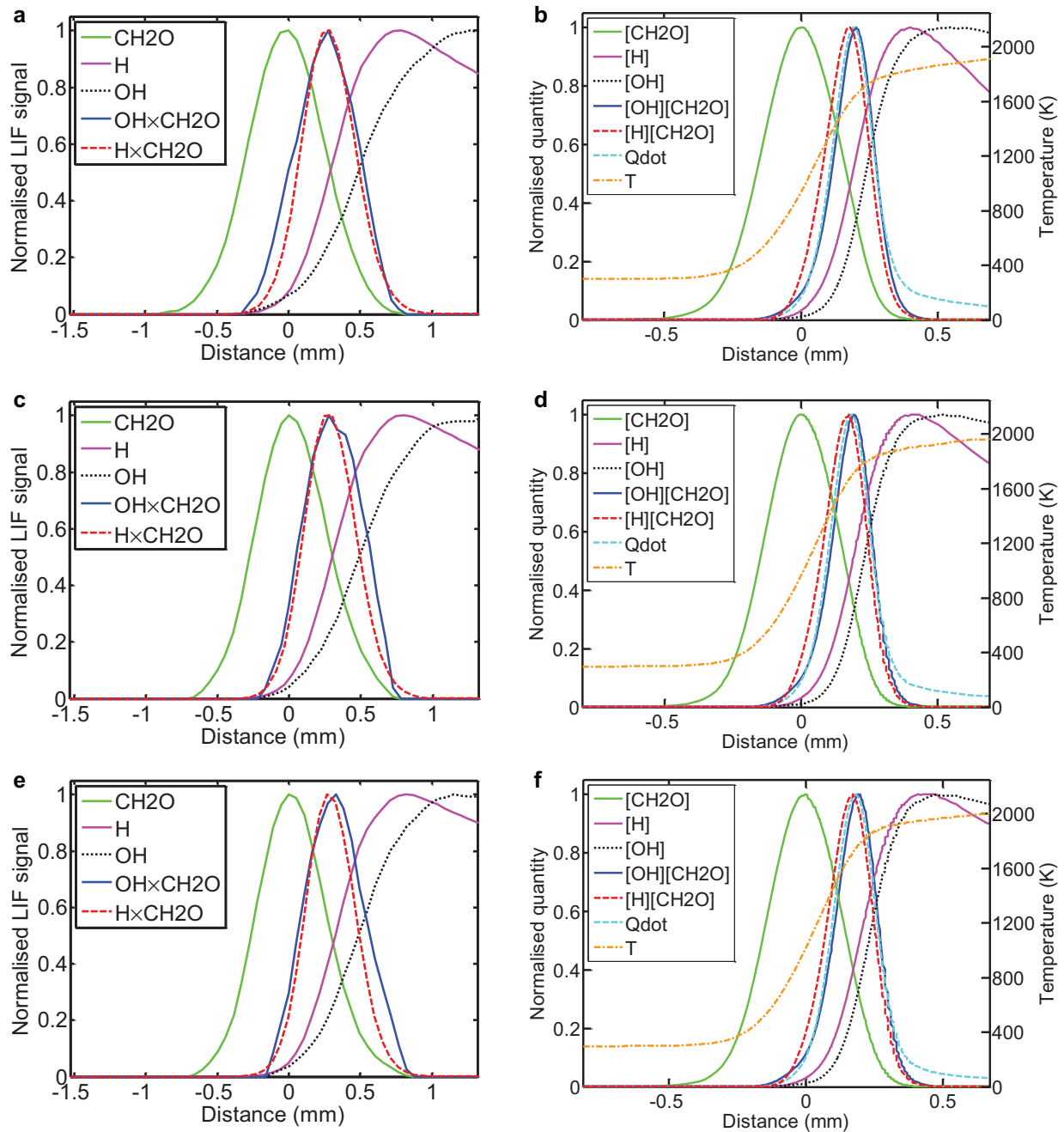
Fig. 5. Profiles of radicals at different equivalence ratios: (a), (c) and (e) are the experimental mean LIF profiles for ϕ = 0.9, 1.0 and 1.1 respectively; (b), (d) and (f) are the calculated molar concentration profiles (along with the temperature and the heat release rate) for ϕ = 0.9, 1.0, and 1.1 respectively.

In addition to the concentration profiles, the temperature profile is also presented for modelled flame in Fig. 5(b), (d), and (f). The temperature increases sharply with the rise in the CH_2O concentration. The temperature gradient decreases in the region of overlap of the CH_2O/OH and CH_2O/H. The temperature does not peak in the region of overlap, instead it reaches a maximum value asymptotically well downstream of the flame ($x \sim 20$ mm). Hence, we evaluate a representative mean temperature T_{mean} for the region corresponding to the FWHM of the simulated HRR (Qdot) profile (Δx) for the respective flames. The gas temperature of an individual flame condition changes over 28–34% across the respective Δx region, for the ϕ = 0.8–1.1 range. This variation appears significant; however, the corresponding representative temperature T_{mean} varies only by 10% across the different flame conditions over the

ϕ = 0.8–1.1 range. This 10% variation is not significant considering the given range of equivalence ratio. Its implications on the deduced HRR are carefully assessed in Section 3.2. The significance of this variation is more relevant to an integrated heat release rate. Therefore, the T_{mean} variation with equivalence ratio is presented subsequently in Section 3.2.

The [H] × [CH_2O] and [OH] × [CH_2O] profiles are in good agreement with the Qdot profile, as shown in Fig. 5(b), (d), and (f). This demonstrates the feasibility of the H × CH_2O LIF based HRR imaging technique.

The spatial variation of Qdot (HRR from the simulation) is compared to the product of concentrations in Fig. 6 for the computed flames for ϕ = 0.8, 0.9, 1.0, and 1.1. The quantities are normalised using their respective peak values. These plots present the spatial
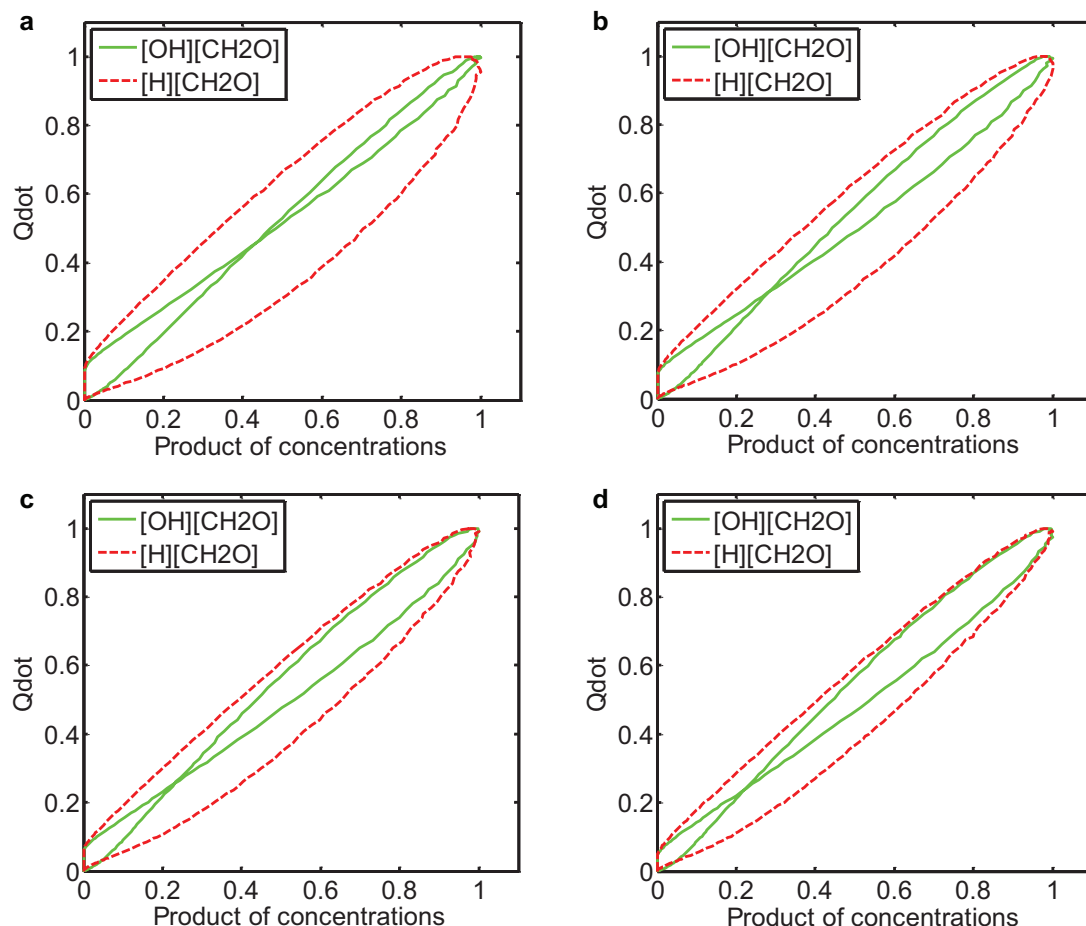
Fig. 6. Simulated HRR (Qdot) is compared against that deduced from the products of $[OH] \times [CH_2O]$ and $[H] \times [CH_2O]$ for flames of different equivalence ratios: (a) $\phi = 0.8$, (b) $\phi = 0.9$, (c) $\phi = 1.0$, and (d) $\phi = 1.1$.

correlation between Qdot and the product of concentrations. Such plots are highly sensitive to minute spatial changes in the concentration profiles, which can be inferred by comparing Fig. 5(b), (d), and (f) with Fig. 6(b), (c), and (d) respectively. The $[OH] \times [CH_2O]$ marker performs superior to the $[H] \times [CH_2O]$ within entire ϕ range of 0.8–1.1. The accuracy of the $[H] \times [CH_2O]$ marker improves monotonically with equivalence ratio, within the above ϕ range. Both the $[OH] \times [CH_2O]$ and $[H] \times [CH_2O]$ products show a good spatial correlations with Qdot, as observed from Fig. 5(b), (d), and (f). However, the $[OH] \times [CH_2O]$ marker is more accurate than $[H] \times [CH_2O]$, although the difference is not significant for practical purposes. The typical difference is estimated by following the location of the Qdot profile at half maximum along the rising edge. At $\phi = 1.0$, the difference between the $[OH] \times [CH_2O]$ and Qdot profiles is 0.008 mm, whereas this difference is 0.024 mm for $[H] \times [CH_2O]$. This suggests that the $[H] \times [CH_2O]$ product can also be used to mark the spatial distribution of HRR similar to the $[OH] \times [CH_2O]$ product in laminar premixed methane flames.

It is important to note that the product of concentrations cannot entirely represent the rate of a salient elementary reaction because of the associated temperature dependence of its reaction rate through the specific rate constant. The temperature dependence of the rate of an elementary reaction can change the perspective obtained using the product of concentrations. This becomes apparent if one compares the perception gathered from Fig. 6 to the conclusion in [25]. In the present work, the Qdot obtained from laminar flame calculation forms the absolute reference to evaluate the accuracy of each technique. If such information is unavailable, then

the HRR markers based on concentration need to be treated with caution. It is necessary to examine the correlation between the choice of reaction rate and the HRR, along with the temperature sensitivity of the rate constant and the LIF signals. This analysis is performed for the present markers in the next section.

3.2. Effect of temperature variation on the HRR technique

The impact of variation in temperature on the LIF signals and specific rate constants is estimated in this section. The temperature dependence of the LIF signal is evaluated for each species (H-atom, OH, and CH_2O) as explained earlier in Section 2.2. The rate constant for the elementary reaction corresponding to the OH $\times$ CH_2O marker is represented by $k_1(T)$ and the corresponding combined temperature dependence of the LIF signal is $f_1(T)$. Similarly, $k_2(T)$ and $f_2(T)$ represent the rate constant and the combined temperature dependence of LIF respectively, for the H $\times$ CH_2O marker. $f_1(T)$ and $f_2(T)$ are compared with $k_1(T)$ and $k_2(T)$, respectively, for three equivalence ratios $\phi = 0.7, 0.9$, and 1.1 in Fig. 7. The values of $k(T)$ and $f(T)$ are evaluated within the FWHM of the Qdot profile (Δx), similar to the T_{mean}. Also, these values are normalised with their respective values at T_{mean}.

$f_1(T)$ for the OH $\times$ CH_2O marker does not closely mimic $k_1(T)$, whereas $f_2(T)$ and $k_2(T)$ are in better agreement for the H $\times$ CH_2O marker for all the three equivalence ratios. Consequently, the H $\times$ CH_2O marker is expected to provide better estimates of HRR than the OH $\times$ CH_2O marker. However, note that there is some uncertainty in modelling of the CH_2O LIF signal and its temperature
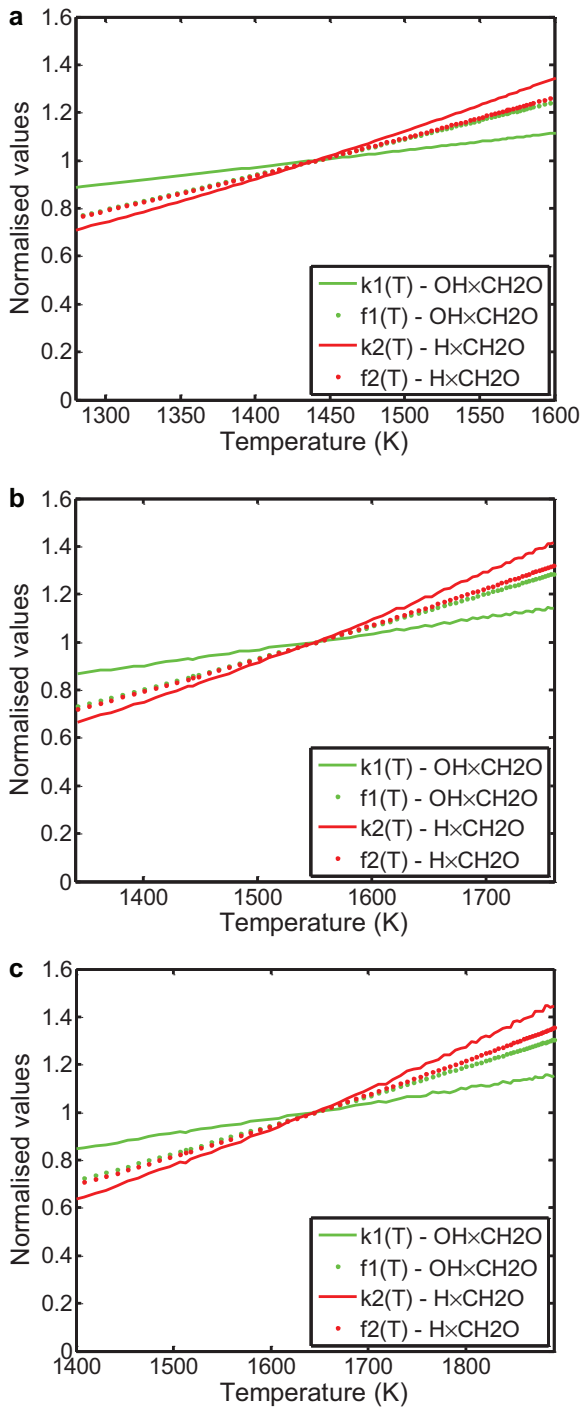
Fig. 8. Specific reaction rate constant evaluated at T_{mean} for different equivalence ratios.

than that of the OH × CH_2O marker. This explains the behaviour in Fig. 6, where Qdot is observed to correlate better with the [OH] × [CH_2O] product than the [H] × [CH_2O] product. The dependence of the rate constants (evaluated at T_{mean}) on the equivalence ratio is also presented in Fig. 8. The variation in the rate constant of the H + CH_2O reaction is greater than that of the OH + CH_2O reaction.

The temperature dependencies of the OH × CH_2O and H × CH_2O LIF markers are nearly identical for a given equivalence ratio. Additionally, the trends in $f_1(T)$ and $f_2(T)$ do not change significantly across a wide range of equivalence ratio (0.7–1.1). Thus, the product of radical concentrations evaluated using the LIF technique is not expected to have a significant bias attributed to the temperature dependence for these two markers. Therefore, the use of the LIF technique may be sufficient to represent the relative product of concentrations, as in the present work.

Next, we assess the correlation between the simulated HRR (Qdot) and the reaction rate using the laminar flame calculations. The reaction rate is evaluated by taking the product of the specific reaction rate constant k and the molar concentrations of the corresponding species. Figure 9 shows the plots for three equivalence ratios. At $\phi = 0.7$ and 1.1, the reaction rates for the OH × CH_2O and the H × CH_2O markers correlate with heat release rate to nearly the same extent. However, for $\phi = 0.9$, the reaction rate for the H × CH_2O marker appears to perform better than that for the OH × CH_2O marker. Overall, the reaction rates for both the OH × CH_2O and the H × CH_2O markers correlate strongly with Qdot over a wide range of ϕ (0.7–1.1). Thus, the reaction rate can be considered as a faithful indicator of the HRR. However, with the LIF technique, only the species concentrations are accessible. Thus, the temperature dependencies of both the parameters $k(T)$ and $f(T)$ (refer Fig. 7) govern the performance of both the HRR markers.

3.3. Integrated HRR variation with equivalence ratio

In Section 3.1, the normalised values of the Qdot, [H] × [CH_2O] and [OH] × [CH_2O] products are used to compare the spatial correlations. In order to obtain the variation of the HRR with respect to equivalence ratio, the [H] × [CH_2O] and [OH] × [CH_2O] profiles are spatially integrated. As stated earlier (in Section 3.1), the normalised mean temperature T_{mean} for the region corresponding to the FWHM of Qdot profile is plotted for $\phi = 0.6$–1.1 in Fig. 7. Over this range of equivalence ratio, T_{mean} changes by 18%, whereas it varies only by 10% in the range $\phi = 0.8$–1.1. Therefore, the influence of temperature variation across equivalence ratios is not expected to be significant.

Fig. 7. Variation of the rate constant $k(T)$ and the combined temperature dependence $f(T)$ for the two different markers at various equivalence ratios: (a) $\phi = 0.7$, (b) $\phi = 0.9$, and (c) $\phi = 1.1$.

dependence. Nevertheless, the performance of OH × CH_2O technique could be enhanced by selecting a different OH LIF excitation scheme to mimic $k_1(T)$. Such flexibility is readily unavailable for H-atom transitions. Although multiple excitation schemes are possible for CH_2O LIF, the one corresponding to the third-harmonic of a Nd:YAG laser is usually the preferred choice.

The rate constant for the OH + CH_2O reaction, $k_1(T)$, shown in Fig. 7 is fairly constant (varies within 20%) in the temperature range of interest for a given equivalence ratio. However, for the H × CH_2O marker, the variation of the rate constant $k_2(T)$ is greater
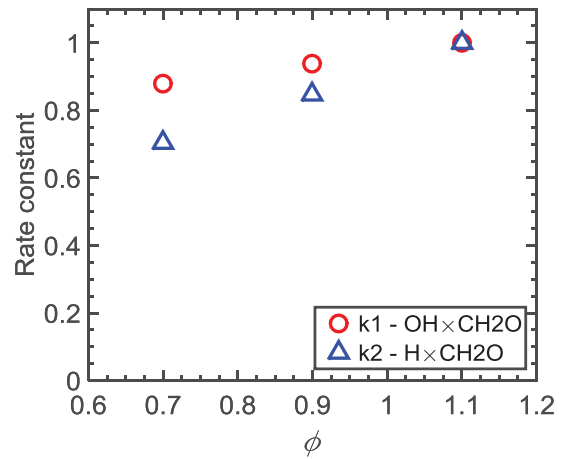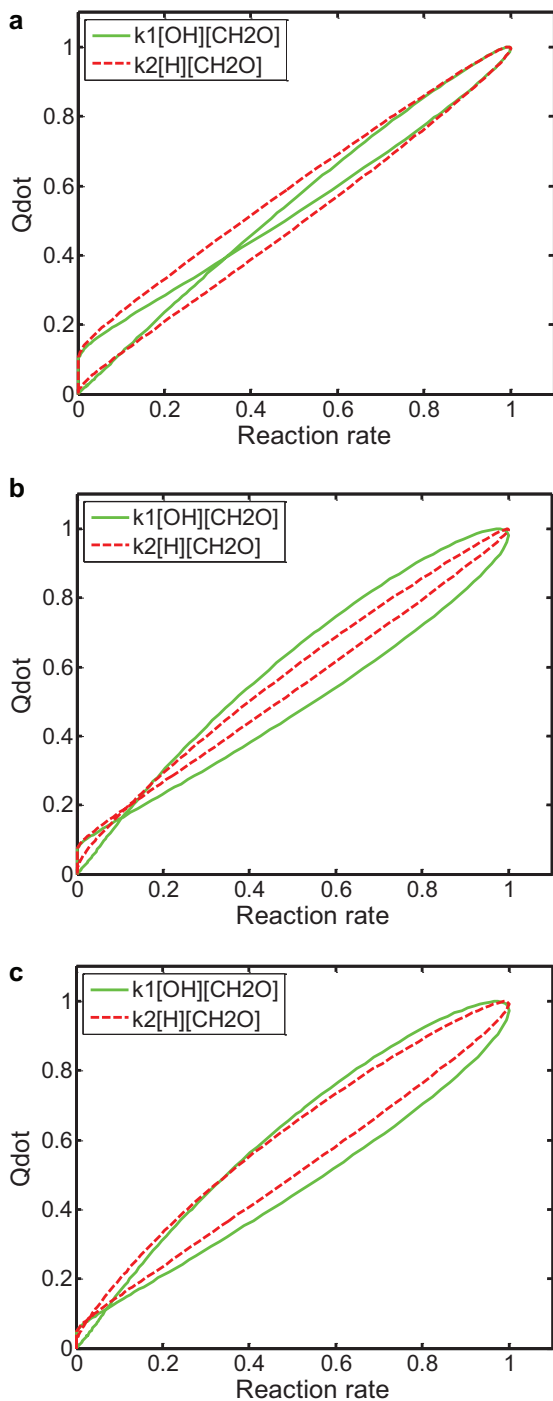
Fig. 9. Simulated HRR (Qdot) with the reaction rate at different equivalence ratios: (a) $\phi = 0.7$, (b) $\phi = 0.9$, and (c) $\phi = 1.1$.

Fig. 10. Variation of the spatially integrated HRR with equivalence ratio.

by either of these two markers (product pairs of the scalar concentrations) calculated from the simulated flames. Both the H × CH_2O and the OH × CH_2O LIF products based HRR trends peak at $\phi = 1.1$, where the flame speed is also known to peak [39–41]. The agreement between the trends of the LIF based product and the simulated concentration product is better for the H × CH_2O marker than that for the OH × CH_2O marker. This is because of the closer match between $k(T)$ and $f(T)$ for the H × CH_2O than for the OH × CH_2O, as shown earlier in Fig. 7. Nevertheless, the trend of the OH × CH_2O LIF variation between $\phi = 1.0$ and 1.1 is in better agreement with the simulated HRR (Qdot) than that of the H × CH_2O LIF. On the other hand, in the $\phi = 0.8$–1.0 range, both the techniques appear to be equally good.

4. Conclusions

The present work demonstrates the feasibility of H × CH_2O LIF as an alternative surrogate marker for HRR imaging for the first time. This technique is compared with the now classical OH × CH_2O LIF based technique. The performance of each of the two markers is assessed based on the following two aspects: (1) spatial correlation between the local HRR and the marker at a given equivalence ratio, and (2) relative variation of the total HRR with equivalence ratio.

The spatial performance of the two markers is similar, with the OH-based marker exhibiting a relatively better behaviour because of the weaker temperature sensitivity of the rate constant of its elementary reaction. However, the integrated HRR deduced with this marker shows certain sensitivity to the equivalence ratio, whereas the H-atom based marker is only weakly sensitive to the equivalence ratio. The trend in the spatial distribution of HRR agrees well with the one-dimensional flame calculations. The H × CH_2O LIF based HRR profile spatially correlates well with that of the OH × CH_2O LIF. The trends in the spatial variation of both the H × CH_2O LIF and the OH × CH_2O LIF agree with the corresponding products of species concentrations obtained from the simulations. The one-dimensional flame calculations suggest that the spatial correlation between the HRR and the OH × CH_2O based marker is better than the H × CH_2O marker by a small margin for $\phi = 0.8$–1.1. Yet, the error associated with the choice of H × CH_2O is well below sub-millimetre (typically a few tens of microns), which is acceptable for practical purposes.

The variation of the spatially integrated (total) heat release rate with equivalence ratio is also presented. The trend in the variation of the simulated HRR is in closer agreement with the integrated OH × CH_2O LIF than that of the integrated H × CH_2O LIF, especially

Figure 10 compares the spatially integrated HRR estimates deduced from the experiments and simulations. The simulated values are also plotted for the $\phi = 0.6$ and 0.7 flames to visualise the trend. All the quantities are normalised with their respective peak values. Note that in the present work no quantitative estimates of HRR are intended; instead trends in the HRR are investigated. As observed from the plot, even in the case of the simulations, Qdot does not agree with either of the products ([OH] × [CH_2O] or [H] × [CH_2O]), because the total HRR depends on the *rates* of certain important elementary reactions [25]. However, the trend in the variation of the total HRR with equivalence ratio is represented well
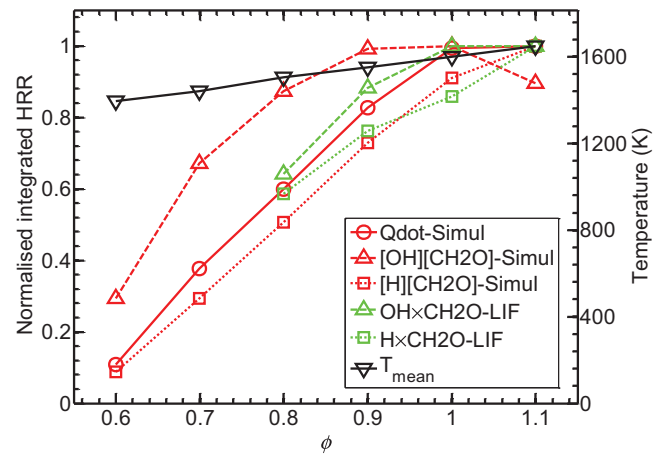
for $\phi = 1.0$–1.1. However, in the $\phi = 0.8$–1.0 range, both the markers perform equally well. For the spatial distribution of HRR, both the OH $\times$ CH$_2$O LIF and the H $\times$ CH$_2$O LIF are suitable markers for the present flames over the entire range of $\phi = 0.8$–1.1. The spatial distribution of HRR is of great interest for studying turbulent combustion modelling, combustion noise, and instabilities. These topics are of central value specifically for gas turbine combustors operating on lean-burn concepts using fossil and alternative fuels. At fuel-lean conditions, which are of practical interest, the total HRR estimate based on either the OH $\times$ CH$_2$O or H $\times$ CH$_2$O LIF appears to be equally good for the conditions investigated in this study. The temperature dependence can be controlled in the former technique by tuning the excitation wavelength for different rotational transitions of OH, which is not readily applicable for H-atom transitions. Additionally, planar single-shot measurement with the H $\times$ CH$_2$O LIF technique is significantly challenging at this time due to low H-atom LIF signal, which is attributed to the two-photon excitation process. Thus, for the present premixed flame conditions, the OH $\times$ CH$_2$O LIF technique is more practical as compared to the H $\times$ CH$_2$O LIF. Nevertheless, with improvements to H-atom LIF techniques and diagnostic equipment, the H-atom based method may prove to be reliable for stratified flames of practical interest, because of weak sensitivity of the rate of reaction of the H $\times$ CH$_2$O marker to variation in the stoichiometry, as has been shown in [25]. Furthermore, the H-atom based method is expected to have wider applications such as in ignition kernel developments and combustion of low-carbon fuel. The validity and feasibility of the H $\times$ CH$_2$O LIF marker for a wider range of equivalence ratios than considered here and turbulent flames needs further assessment with elaborate experimental measurements.

Acknowledgments

References

[1] D. Bradley, 'Hot spots' and gasoline engine knock, J. Chem. Soc. Faraday Trans. 92 (1996) 2959–2964.

[2] O. Tuncer, S. Acharya, J. Cohen, A. Banaszuk, Side air-jet modulation for control of heat release and pattern factor, Combust. Sci. Technol. 177 (2005) 1339–1364.

[3] T. Poinsot, D. Veynante, F. Bourienne, S. Candel, E. Esposito, J. Surget, Initiation and suppression of combustion instabilities by active control, Symp. (Int.) Combust. 22 (1988) 1363–1370.

[4] J.P. Hathout, M. Fleifil, A.M. Annaswamy, A.F. Ghoniem, Heat-release actuation for control of mixture-inhomogeneity-driven combustion instability, Proc. Combust. Inst. 28 (2000) 721–730.

[5] S. Candel, Combustion dynamics and control: progress and challenges, Proc. Combust. Inst. 29 (2002) 1–28.

[6] T. Lieuwen, Modeling premixed combustion-acoustic wave interactions: a review, J. Propul. Power 19 (2003) 765–781.

[7] B.O. Ayoola, R. Balachandran, J.H. Frank, E. Mastorakos, C.F. Kaminski, Spatially resolved heat release rate measurements in turbulent premixed flames, Combust. Flame 144 (2006) 1–16.

[8] S.L. Bragg, Combustion noise, J. Inst. Fuel 36 (1963) 12–16.

[9] N. Swaminathan, G. Xu, A.P. Dowling, R. Balachandran, Heat release rate correlation and combustion noise in premixed flames, J. Fluid Mech. 681 (2011) 80–115.

[10] P.H. Paul, H.N. Najm, Planar laser-induced fluorescence imaging of flame heat release rate, Symp. (Int.) Combust. 27 (1998) 43–50.

[11] J.G. Lee, D.A. Santavicca, Experimental diagnostics for the study of combustion instabilities in lean premixed combustors, J. Prop. Power 19 (2003) 735–750.

[12] Y. Hardalupas, M. Orain, Local measurements of the time-dependent heat release rate and equivalence ratio using chemiluminescent emission from a flame, Combust. Flame 139 (2004) 188–207.

[13] Y. Hardalupas, C.S. Panoutsos, A.M.K.P. Taylor, Spatial resolution of a chemiluminescence sensor for local heat-release rate and equivalence ratio measurements in a model gas turbine combustor, Exp. Fluids 49 (2010) 883–909.

[14] H.N. Najm, P.H. Paul, C.J. Mueller, P.S. Wyckoff, On the adequacy of certain experimental observables as measurements of flame burning rate, Combust. Flame 113 (1998) 312–332.

[15] J. Kiefer, Z.S. Li, T. Seeger, A. Leipertz, M. Aldén, Planar laser-induced fluorescence of HCO for instantaneous flame front imaging in hydrocarbon flames, Proc. Combust. Inst. 32 (2009) 921–928.

[16] B. Zhou, J. Kiefer, J. Zetterberg, Z. Li, M. Aldén, Strategy for PLIF single-shot HCO imaging in turbulent methane/air flames, Combust. Flame 161 (2014) 1566–1574.

[17] S. Böckle, J. Kazenwadel, T. Kunzelmann, D.-I. Shin, C. Schulz, J. Wolfrum, Simultaneous single-shot laser-based imaging of formaldehyde, OH, and temperature in turbulent flames, Proc. Combust. Inst. 28 (2000) 279–286.

[18] R. Balachandran, B.O. Ayoola, C.F. Kaminski, A.P. Dowling, E. Mastorakos, Experimental investigation of the nonlinear response of turbulent premixed flames to imposed inlet velocity oscillations, Combust. Flame 143 (2005) 37–55.

[19] R.L. Gordon, A.R. Masri, E. Mastorakos, Heat release rate as represented by [OH] $\times$ [CH$_2$O] and its role in autoignition, Combust. Theor. Model. 13 (2009) 645–670.

[20] J. Kariuki, A. Dowlut, R. Yuan, R. Balachandran, E. Mastorakos, Heat release imaging in turbulent premixed methane–air flames close to blow-off, Proc. Combust. Inst. 35 (2015) 1443–1450.

[21] R. Yuan, J. Kariuki, A. Dowlut, R. Balachandran, E. Mastorakos, Reaction zone visualisation in swirling spray n-heptane flames, Proc. Combust. Inst. 35 (2015) 1649–1656.

[22] A. Fayoux, K. Zähringer, O. Gicquel, J.C. Rolon, Experimental and numerical determination of heat release in counterflow premixed laminar flames, Proc. Combust. Inst. 30 (2005) 251–257.

[23] A. Gazi, G. Vourliotakis, G. Skevis, M.A. Founti, Assessment of chemical markers for heat-release rate correlations in laminar premixed flames, Combust. Sci. Technol. 185 (2013) 1482–1508.

[24] Y. Minamoto, N. Swaminathan, Scalar gradient behaviour in MILD combustion, Combust. Flame 161 (2014) 1063–1075.

[25] Z.M. Nikolaou, N. Swaminathan, Heat release rate markers for premixed combustion, Combust. Flame 161 (2014) 3073–3084.

[26] L. Gasnot, P. Desgroux, J.F. Pauwels, L.R. Sochet, Improvement of two-photon laser induced fluorescence measurements of H- and O-atoms in premixed methane/air flames, Appl. Phys. B 65 (1997) 639–646.

[27] W.D. Kulatilaka, J.H. Frank, T.B. Settersten, Interference-free two-photon LIF imaging of atomic hydrogen in flames using picosecond excitation, Proc. Combust. Inst. 32 (2009) 955–962.

[28] W.D. Kulatilaka, B.D. Patterson, J.H. Frank, T.B. Settersten, Analysis of 205-nm photolytic production of atomic hydrogen in methane flames, Appl. Phys. B 97 (2009) 227–242.

[29] W.D. Kulatilaka, B.D. Patterson, J.H. Frank, T.B. Settersten, Comparison of nanosecond and picosecond excitation for interference-free two-photon laser-induced fluorescence detection of atomic hydrogen in flames, App. Opt. 47 (2008) 4672–4683.

[30] W.D. Kulatilaka, J.R. Gord, V.R. Katta, S. Roy, Photolytic-interference-free, femtosecond two-photon fluorescence imaging of atomic hydrogen, Opt. Lett. 37 (2012) 3051–3053.

[31] R.J. Kee, J.F. Grcar, M. Smooke, J.A. Miller, PREMIX: A FORTRAN program for modeling steady one dimensional premixed flames, Report No. SAND85-8240, Sandia National Laboratories, Livermore, CA, USA, 1985.

[32] G.P. Smith, D.M. Golden, M. Frenklach, N.W. Moriarty, B. Eiteneer, M. Goldenberg, C.T. Bowman, R.K. Hanson, S. Song, W.C. Gardiner, V.V. Lissianski, Z. Qin. http://www.me.berkeley.edu/gri_mech, (accessed 07.07.14).

[33] "Chemical-kinetic mechanisms for combustion applications", San Diego Mechanism web page, Mechanical and aerospace engineering (combustion research), University of California San Diego (http://combustion.ucsd.edu).

[34] A.C. Eckbreth, Laser diagnostics for combustion temperature and species, 2nd Ed., Gordon and Breach Publishers, Amsterdam, 1996.

[35] N.L. Garland, D.R. Crosley, On the collisional quenching of electronically excited OH, NH and CH in flames, Symp. (Int.) Combust. 21 (1986) 1693–1702.

[36] D. Stepowski, M.J. Cottereau, Study of the collisional lifetime of hydroxyl ($2\Sigma+$, $v'=0$) radicals in flames by time-resolved laser-induced fluorescence, Combust. Flame 40 (1981) 65–70.

[37] B.O. Ayoola, Laser-based measurement of heat release rate and temperature in turbulent premixed flames Doctoral thesis, University of Cambridge, 2005.

[38] D. Kyritsis, V. Santoro, A. Gomez, The effect of temperature correction on the measured thickness of formaldehyde zones in diffusion flames for 355 nm excitation, Exp. Fluids 37 (2004) 769–772.

[39] G.E. Andrews, D. Bradley, The burning velocity of methane-air mixtures, Combust. Flame 18 (1972) 133–153.

[40] C.M. Vagelopoulos, F.N. Egolfopoulos, C.K. Law, Further considerations on the determination of laminar flame speeds with the counterflow twin-flame technique, Combust. Flame 32 (1994) 1341–1347.

[41] G. Yu, C.K. Law, C.K. Wu, Laminar flame speeds of hydrocarbon + air mixtures with hydrogen addition, Combust. Flame 63 (1986) 339–347.